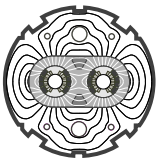

LHC Project Note 258

14 June 2001

Keith.Potter@cern.ch

Methodical study of the machine induced background formation in the IR8 of LHC

I. Azhgirey*, I. Baishev*, K.M. Potter and V. Talanov*

Keywords: losses, cascade, muon

Summary

In this work we estimate the machine induced background, resulting from the proton losses upstream and downstream of insertion region IR8, for the lattice version 6.1.

Introduction

Fluxes of the secondary particles, induced by proton losses upstream and downstream of the interaction points, affect the radiation environment in the corresponding insertion regions and can contribute to the detector backgrounds [1]. The characteristic feature of these secondary fluxes, or *machine induced background*, is that its value is proportional to the machine beam current, while the particle fluxes, produced in the proton-proton collisions, scale with the luminosity at a particular interaction point. This means that the relative effect of the machine induced background depends on the machine operating conditions and is different for different run scenarios.

Secondary particle cascades can be initiated in the insertion region in the set of different physical processes. The origins of these secondary fluxes are listed in Table 1. The generic proton losses are the interactions of the beam protons with residual gas nuclei, resulting in multiple production of secondary particles. Their distribution along the machine thus reflects the distribution of the residual gas pressure. These interactions can be divided into two types, inelastic and elastic ones. The secondaries from inelastic interactions have in general a resulting momentum significantly smaller than the beam particles, and can not be transported through the magnetic structure of the machine. In the arcs and dispersion suppressors, being enclosed by the machine tunnel, these particles are stopped due to the curvature of the accelerator ring and affect the radiation field mainly in the regions close

*Institute for High Energy Physics, Protvino, Russia.
Member of the Russian collaboration to the LHC Project.

Inelastic scattering
Beam protons collisions with the nuclei of the residual gas in the arc cells, dispersion suppressors and straight sections, resulting in multiple production of secondaries
Elastic scattering
Elastic and also inelastic proton–nucleus collisions, having a leading proton in the final state
Cleaning inefficiency
Proton out-scattering from the collimators followed not by absorption in the collimators or in other elements of the cleaning system but rather by subsequent proton loss somewhere downstream of the cleaning system
Collisions in the interaction points
Proton–proton collisions in high luminosity interaction points, which give energetic protons, transported to and lost in the next insertion region

Table 1: Origins of the machine induced background.

to the point of the original collision. Opposite to this, secondaries produced in elastic interactions have a different behaviour. Elastic collisions of beam particles with the residual gas nuclei give in the final state energetic protons with a momentum much closer to the initial one. These *quasi–beam* particles can successfully travel with the beam long distances through the lattice to interact with the machine equipment far from the point of the primary collision [2].

Thus the choice of the machine length which is necessary to introduce in the simulation of the background, induced by proton losses, as well as how to account for different origins of this background, depends on the position of the studied region in the machine structure.

1 The choice of the studied machine length

The general scheme of the LHC machine is shown at the Figure 1. Expected contributions of the distant sources of the proton losses to the machine induced background in IR8 depend on the beam size limitations in neighbouring insertions. As can be seen from this scheme, the adjacent insertions to IR8 are the betatron cleaning insertion IR7, which is upstream of IP8 for Ring 1, and the high luminosity insertion IR1, which is downstream. The aperture of the inner triplets in IR1 is approximately 20 r.m.s. beam sizes, or 20σ, at $\beta^* = 0.5$ m, while the nominal position of the primary collimators in IR7 is at 6σ. Therefore it can be assumed that the neighbouring insertions separate IR8 from all the distant sources of this kind, while along the length of the Ring 1 sector 78 and Ring 2 sector 81 the beam–gas collisions of this type have to be included in the simulation.

As for the inelastic collisions, taking into account the curvature of the ring, the part of the machine structure including IR8 long straight section together with, on both sides of the insertion region, the dispersion suppressor and one arc cell next to it, was considered sufficient.

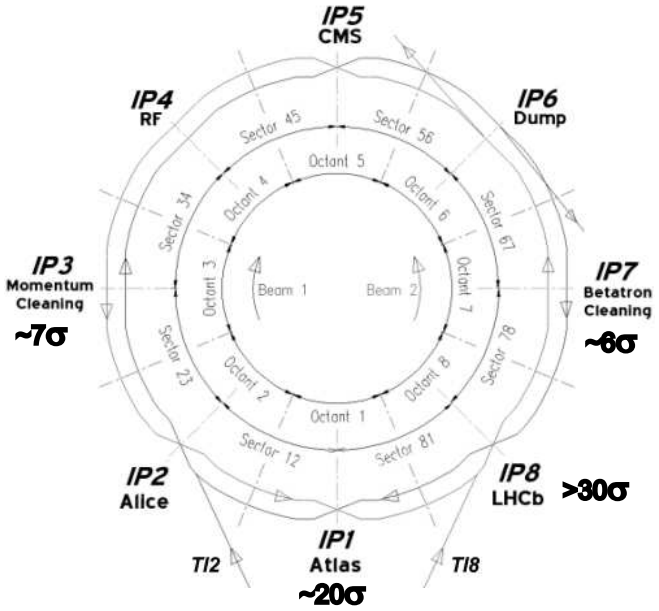

Figure 1: The LHC scheme.

2 The model of the studied section

The layout of the studied LHC section is given in Figure 2. It consists of the long straight section SS8, together with the dispersion suppressor and one arc cell, both upstream and downstream of IP8. The model of the standard arc cell was built of two similar halfs, with three 14.2 m twin aperture dipoles followed by one 3.1 m quadrupole in each. Two types of LHC main dipoles MBA and MBB, used for B13 and B12 magnetic elements, were not distinguished in the simulations and considered to be identical. The dispersion suppressor part consisted of four quadrupoles, positioned in pairs between eight dipoles, which were the same dipoles as in the arc. For the Q8—Q10 quadrupoles, which differ only in length, the common model was used, while Q11 was described as a combination of main quadrupole MQ and long trim MQTL quadrupole models.

The downstream part of the straight section consisted of the low–β quadrupole triplet Q1—Q3, a pair of separation dipoles, single aperture D1 and twin aperture D2, injection elements and matching quadrupole section Q4—Q7. The upstream part had the same layout except that there were no injection elements. The two odd inner triplet magnets, Q1 and Q3, were represented by the same model, and another one was used for the two sections of Q2 to account for the enlarged coils and shrinking cylinder diameters. Also a distinct model was used for Q5, which, being of the same type as Q6 and Q7, had a different operational temperature. The distance from the front surface of the last inner triplet quadrupole Q1 to the interaction point was 23 m, and three warm box–like compensating magnets, two upstream and one downstream from IP8, were installed around the interaction point, with the dimensions according to the data available at the moment of calculations.

Geometry for the particle cascade simulations was built according to several data sources. LHC lattice version 6.1 was used to extract the positions and nominal field values for the

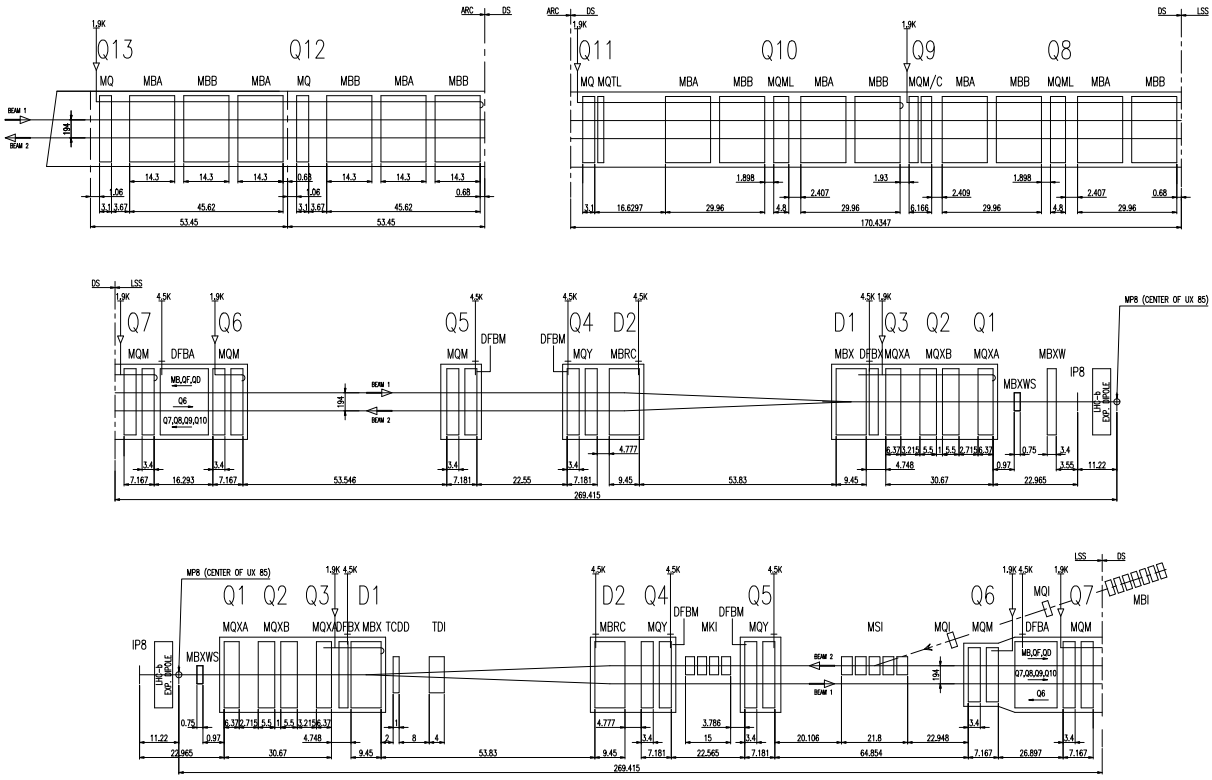

Figure 2: The layout of the studied LHC section: arc cell and upstream dispersion suppressor DS8L, together with the left and right part of the long straight section, SS8L and SS8R (the last with the injection elements) (optics version 6.3).

magnets. The magnetic field values which were used for the elements in the arc cell and dispersion suppressor are given in Table 2, and Table 3 gives the same quantities for the elements in the upstream and downstream parts of the straight section. An important point is that the optics of the straight section in IR8 is designed to be flexible enough to allow a wide range of beta-function values 1 m $\leq \beta^* \leq$ 50 m in IP8 [3]. We choose the number of $\beta^* = 10$ m as the basic one for the study, since the separation scheme in IR8 at this value is valid for machine operation at both collision and injection [4]. We also consider two more β^* options of 1 m and 50 m, in order to study the formation of the machine induced background at the commissioning stage in the first case, and at the high β^* values in the last. As can be seen from Table 3, in the simulations magnetic field was switched off in the orbit correctors, associated with the magnets from Q3 to Q6, thus corresponding to the case of an ideal machine, without imperfections.

Parameters of the magnets, taken from the LHC lattice description, were supplemented by the dimensions of the geometrical apertures of the magnetic elements and drifts in the studied region, according to [5], with the necessary updates for the lattice version 6.1 [6]. The values, used for the straight section elements, are also given in Table 3. Two multiplied numbers in this table represent the presence of the beam screen in the corresponding element, while a single number denotes the inner radius of the cold bore in the magnet. These numbers

Element name	Arc cell β^* option			Element name	DS β^* option		
	1 m	10 m	50 m		1 m	10 m	50 m
QTQF13	1.0644	0.1805	1.0176	QF11	2.0963	2.0688	2.0688
QF13	2.0963	2.0688	2.0688	QTQF11	0.1114	0.0914	0.3435
B13C	8.3274	8.3274	8.3274	B11B	8.3274	8.3274	8.3274
B13B	8.3274	8.3274	8.3274	B11A	8.3274	8.3274	8.3274
B13A	8.3274	8.3274	8.3274	QD10	-1.6306	-1.5188	-1.6672
QTQD12	0.5541	0.5686	1.0665	B10B	8.3274	8.3274	8.3274
QD12	-1.9536	-1.9793	-1.9793	B10A	8.3274	8.3274	8.3274
B12C	8.3274	8.3274	8.3274	QF9	1.4554	1.4272	1.6328
B12B	8.3274	8.3274	8.3274	B9B	8.3274	8.3274	8.3274
B12A	8.3274	8.3274	8.3274	B9A	8.3274	8.3274	8.3274
				QD8	-1.8583	-1.1324	-1.5049
				B8B	8.3274	8.3274	8.3274
				B8A	8.3274	8.3274	8.3274

Table 2: The used values of the nominal magnetic field, B [T], or nominal gradient, G [T/cm], for the arc cell and dispersion suppressor elements.

are omitted in Table 2, since for the arc cell and dispersion suppressor elements the common value of r2.2×h1.8 was used. The thickness of the beam screen was taken equal to 1 mm, and pure *Fe* as the material. Radial dimensions and beam screen size for the cold drift chamber were taken equal to the sizes of corresponding parts of the connected magnets, except for the drift in Q7—Q6 region, where no beam screen was introduced. As for the warm drift chamber, it was assumed to be built of copper and had an inner radius of 5 cm with a thickness of 2 mm.

The diameters of magnet cold bore and coils were taken from the tables of LHC Design — Parameters and Layouts, with the necessary additions on the basis of engineering drawings [7]. The outermost diameter for each magnetic element in the geometry corresponded to the diameter of the shrinking cylinder, and the length of the magnet — to the magnetic length. No parts of vacuum and cryogenic equipment around and between the magnets were taken into account, as well as the magnet supports or other supplementary systems. The LHC tunnel model was introduced into the simulation geometry, according to the current design.

3 Particle cascades simulation

Simulation of different physical processes, which lead to the multiple secondary cascades production, was done for the analysis of the machine induced background in IR8. Uniform distribution of the gas pressure along the arcs, dispersion suppressors and straight sections was assumed in the simulations. The history of each particle was started with a beam proton interaction with the residual gas nuclei. Following [8], we considered hydrogen, carbon and oxygen nuclei of the gas. In order to obtain the most realistic representation of the proton losses along the beam line, the type of the residual gas nuclei was scored according to

Element name	Half-aperture [cm]	SS8L β^* option			SS8R β^* option		
		1 m	10 m	50 m	1 m	10 m	50 m
Q7	r2.27×v1.78	1.992	1.536	1.996	1.585	1.364	1.739
CHQ7	r2.27×v1.78	-0.274	0.061	0.004	-0.274	0.061	0.004
CORQ6	r2.5	0.000	0.000	0.000	0.000	0.000	0.000
Q6	r2.5	-1.877	-1.218	-1.268	-1.588	-0.958	-0.963
Q5	r2.5	0.626	1.109	1.276	0.329	0.993	1.155
CORQ5	r2.5	0.000	0.000	0.000	0.000	0.000	0.000
DHQ4	r2.77×h2.28	-0.674	-0.714	-0.866	-0.674	-0.714	-0.866
CORQ4	r2.77×h2.28	0.000	0.000	0.000	0.000	0.000	0.000
Q4	r2.77×h2.28	-0.610	-0.951	-0.761	-0.479	-1.052	-0.864
D2	r3.22×h2.73	3.655	3.655	3.655	3.655	3.655	3.655
D1	r3.47×v2.98	-3.655	-3.655	-3.655	-3.655	-3.655	-3.655
CORQ3	r3.15	0.000	0.000	0.000	0.000	0.000	0.000
Q3	r3.15	2.042	2.200	1.638	2.042	2.200	1.638
Q2	r3.15	-2.042	-2.200	-1.638	-2.042	-2.200	-1.638
CXQ1	r3.15	0.654	0.467	3.269	0.654	0.467	3.269
Q1	r3.15	2.042	2.200	1.638	2.042	2.200	1.638

Table 3: The used half–aperture dimensions and values of the nominal magnetic field, B [T], or nominal gradient, G [T/cm], for the left and right straight section elements.

the values of relative macroscopic cross-sections of inelastic interactions, as given in Table 4. The compositions were different in the cold arc and dispersion suppressor, and warm straight region. The values of these cross–sections were calculated using the most recently published data on the residual gas densities in the different parts of LHC [9], which are given in Table 5, together with the estimated values for the proton–nucleus inelastic interaction at the LHC energy. For the proton–proton inelastic cross–section the value of $\sigma_{in} = 38$ mb was taken as a result of interpolation between ISR measurements [10] and the CDF data [11]. The inelastic cross–sections for p–C^{12} and p–O^{16} interactions were calculated from the theory of multiple scattering [12], which gave the values of 249 mb and 315 mb respectively. We present the results of simulations per unit density of the beam protons with the residual gas nuclei inelastic interactions. Using the numbers, given above, any other reasonable distribution of the residual gas pressure in LHC can be taken into account [13].

Nucleus	Cold Arcs	Warm Straights
H^1	0.029	0.637
C^{12}	0.288	0.160
O^{16}	0.683	0.203

Table 4: The used values of the relative macroscopic inelastic cross–sections.

Elastic and also inelastic proton–nucleus collisions, leading to the production of an energetic proton in the final state, were simulated by the STR00 version of the STRUCT code [14]. These protons were then transported through the lattice to find the point of their

Gas	Cold Arcs, $I = 53$ mA	Warm Straights
H_2	6.1×10^5	4.6×10^6
CH_4	1.1×10^5	9.7×10^4
H_2O	3.5×10^5	—
CO	5.9×10^5	1.7×10^5
CO_2	2.9×10^6	1.0×10^5

Table 5: The assumed values of the gas densities, [mol/cm^3], in the cold arcs and warm straights.

losses. The protons which appeared to be lost in IR8 were then passed to the second stage to simulate the resulting secondary cascades. Inelastic beam–gas scattering on the chosen length of LHC beam, the cascades caused by the lost protons and the transport of the secondaries were simulated by the IHEP MARS program [15]. The overall threshold of 20 MeV on the particle kinetic energy was applied to the simulation of transport for all the particle types. Secondary particles were transported along IR8 up to two scoring planes, positioned at 1 m upstream and 19.9 m downstream of IP8, the first for the particles from Ring 1, and the second for the ones from Ring 2. The trajectory of each particle was cut there and particle characteristics were recorded.

It has to be noted that positioning the second scoring plane at 19.9 m downstream from IP8 means that the secondary particles from the losses in Ring 2 were collected just in front of the surface of the third IR8 compensation magnet MCBWB, at a distance of 3 m from the downstream Q1 magnet. Meanwhile the scoring plane for Ring 1 at 1 m upstream from IP8 was located at 2.55 m from the second IR8 compensation magnet MBXW, and at 22 m from the downstream Q1. This gave the high-angular secondaries from the Ring 2, produced in the region of downstream low–β triplet Q1–Q3, *a priori* a better chance to reach the scoring plane for Ring 2, than for those produced in the same region of Ring 1.

Three chosen β^* values and two rings gave a total of six final sources. These sources of the recorded background particles were then analysed for Ring 1 and 2 separately. Recorded particle characteristics included particle kinetic energy, direction cosines and coordinates of particle track crossing the scoring plane. Each particle track was also tagged with the distance to the IP8 from the point of the primary proton–nucleus collision, and the type of the residual gas nucleus, with which the interaction occurred. Thus the subsequent reconstruction of secondary particle fields in the IR8 is possible, once real residual gas pressure distributions are known.

The results of the simulations are presented in Figures 3–6. The first two figures are for the Ring 1 source and the last two for the Ring 2, showing the particles, generated by proton losses in the LHC Sector 81 and 78, respectively, including those in the dispersion suppressor and straight section. These figures give the number of hadrons and muons, entering the UX85 cavern, as a function of the proton–nucleus interaction distance to the IP8. On top of each figure a sketch of the corresponding machine structure is given. For a better presentation of the results the structure for the dispersion suppressor and arc is drawn in a straight line. The direction of the S axis on these figures corresponds to the Ring 1, with IP8 at zero. As for the results for proton losses in SS8 [2], these distributions are given per unit of linear

density of beam–gas interactions. This means that these profiles are to be folded with the profiles of the residual gas pressure to obtain the absolute values of particle fluxes.

4 Machine induced background in IR8

The presented particle distributions allow a study of the machine induced background in IR8 from two different points of view. One is the relative contribution of the primary proton–nucleus collisions, which occur in a particular region of the machine structure, to the total number of secondary particles, entering the UX85 cavern. Another is the relative difference of the results for the three studied β^* options.

Longitudinal distributions of the number of particles along S axis, entering the UX85 cavern from both sides, reflect the features of both mechanical and magnetic structure of the machine in the region of study. Analysis of longitudinal source dependence shows that the source can be divided into several parts, originating from different section of IR8. The contribution to the source per metre of S axis in the upstream and downstream parts of the straight section is almost constant for all three studied β^* options, both for secondary hadrons and muons. As can be seen from the mechanical layout, the amount of material per metre of the structure to stop the cascade products is relatively low there. At the same time this region features a significant length of bare vacuum chamber for the particles to interact with and then, considering the secondary $\pi^{\pm}$, to have a long space to decay to muons.

In the parts, distant from IP8, the longitudinal distribution for all three β^* values has long tails, falling down with the increasing distance from the interaction point. These tails have a break at the border between dispersion suppressor and the arc cell, where the curvature of the machine ring starts to increase rapidly. The origin of these tails are the elastic and inelastic proton–nucleus collisions, which give in the final state highly energetic protons. Only these *quasi–beam* particles have a chance to be transported by the optics to the region of the inner triplet Q1–Q3, where they will be lost [2], while the low energy secondaries from other origins will be absorbed in the arc and dispersion suppressor elements, and in the walls of the LHC tunnel.

This has its proof in the comparison between distribution for β^* value of 1 m and those for two other options. The optics for $\beta^* = 1$ m appears to be more sensitive to the proton losses, hence the Q1–Q3 region in this case will collect many more particles, which were originally lost quite far away from the inner triplet. This explains the increase in the distant tail of the longitudinal distribution, which is visible for both types of secondaries and both rings in the $\beta^* = 1$ m option, and is less pronounced in the two other cases. For the β^* values of 10 and 50 m these $n(S)$ distributions at the end of the arc cell fall down by more than five orders of magnitude, relative to the mean value, observed in the straight section, and by more than three orders, compared to the values on the border of the dispersion suppressor and straight section. This gives an indication that the length of the chosen region was correct.

Concluding, it has to be noted that, as defined in section 3, all the analysis above is given for uniform distribution of residual gas pressures in the studied region. Introduction of the real gas pressure profile can lead to significant changes in the picture of background formation.

5 Conclusion

Normalising the results to the proton–nucleus interaction rate, estimated from the Table 4 and 5 data, one arrives for the muon flux at the entrance of UX85 cavern to the value of $0.6 \div 2.2 \times 10^5$ particles/s, depending on the LHC ring number and run conditions. These numbers have to be considered as indicative only and are subject to change with the introduction of realistic values for the residual gas densities.

References

[1] I. Azhgirey *et al*, In: One Day Workshop on LHC Backgrounds, March 22, 1996.

[2] I. Baishev *et al*, Proton losses upstream of IP8 of LHC, LHC Project Note (to be published).

[3] O. Bruening, LHC Project Note 193, 1998.

[4] O. Bruening *et al*, LHC Project Report 367, 2000.

[5] J.B. Jeanneret and R. Ostojic, LHC Project Note 111, 1997.

[6] J.B. Jeanneret, private communication.

[7] H. Prin, private communication.

[8] O.B. Malyshev and A. Rossi, LHC Project Report 437, 2000.

[9] A. Mathewson, In: One Day Workshop on LHC Backgrounds, March 22, 1996 .

[10] U. Amaldi *et al*, Nucl. Phys. **B166** (1980) 301.

[11] F. Abe *et al*, Phys. Rev. **D50** (1994) 5518, 5535, 5550.

[12] R.J. Glauber, In: Lectures in Theor. Phys., Interscience Publ. 4, v.1, 315 (1959).

[13] O.B. Malyshev and I.R. Collins, Vacuum Technical Note 99-14, 1999.

[14] I. Baishev *et al.*, SSCL-MAN-0034, Dallas, 1994.

[15] I. Azhgirey and V. Talanov, In: Proc. of XVIII Workshop on Charged Particles Accelerators, Protvino, October 16–20 (2000).

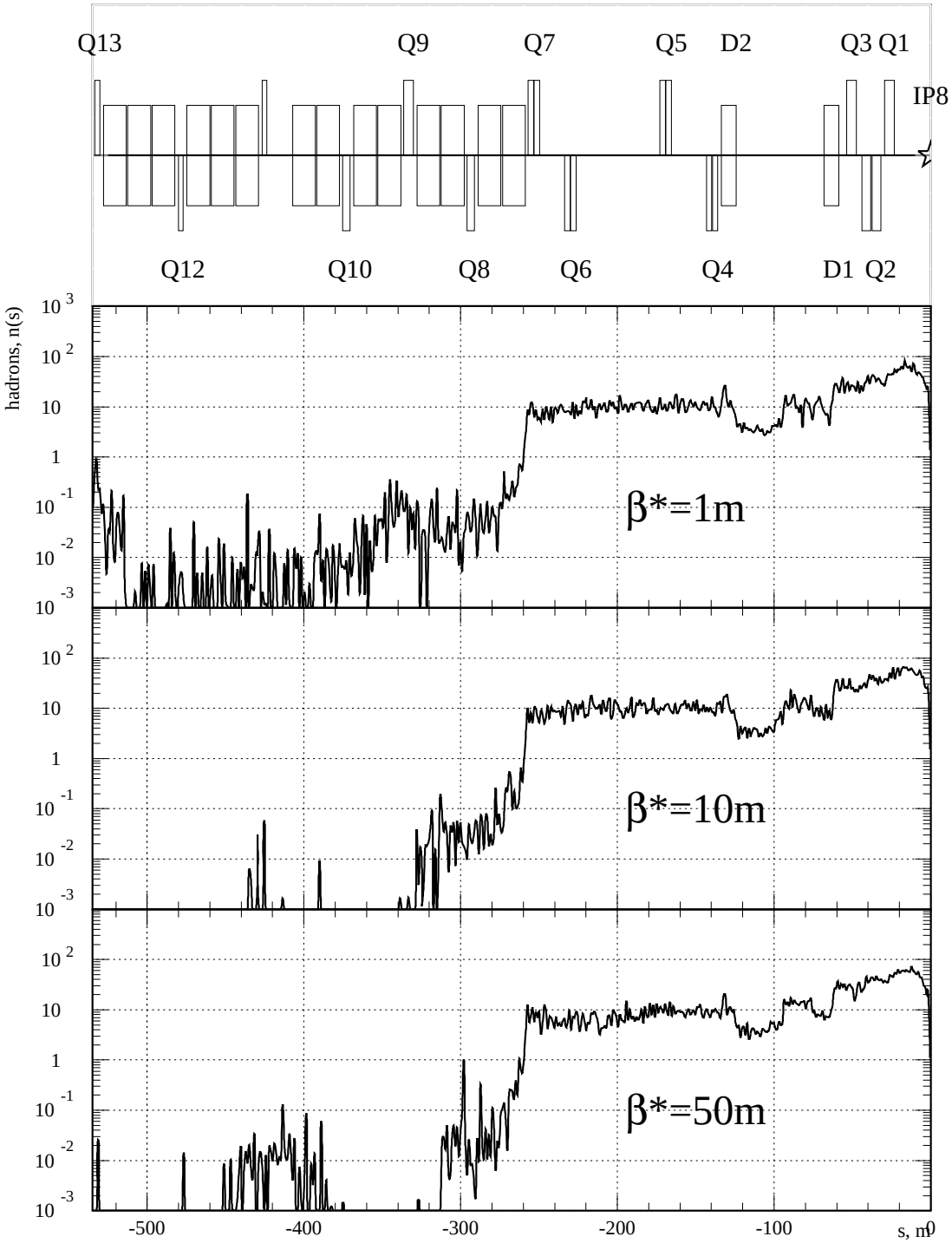

Figure 3: Number of hadrons, entering the UX85 cavern from the IP1 side, as a function of primary proton–nucleus interaction distance to the IP8, given per unit of linear density of beam–gas interactions.

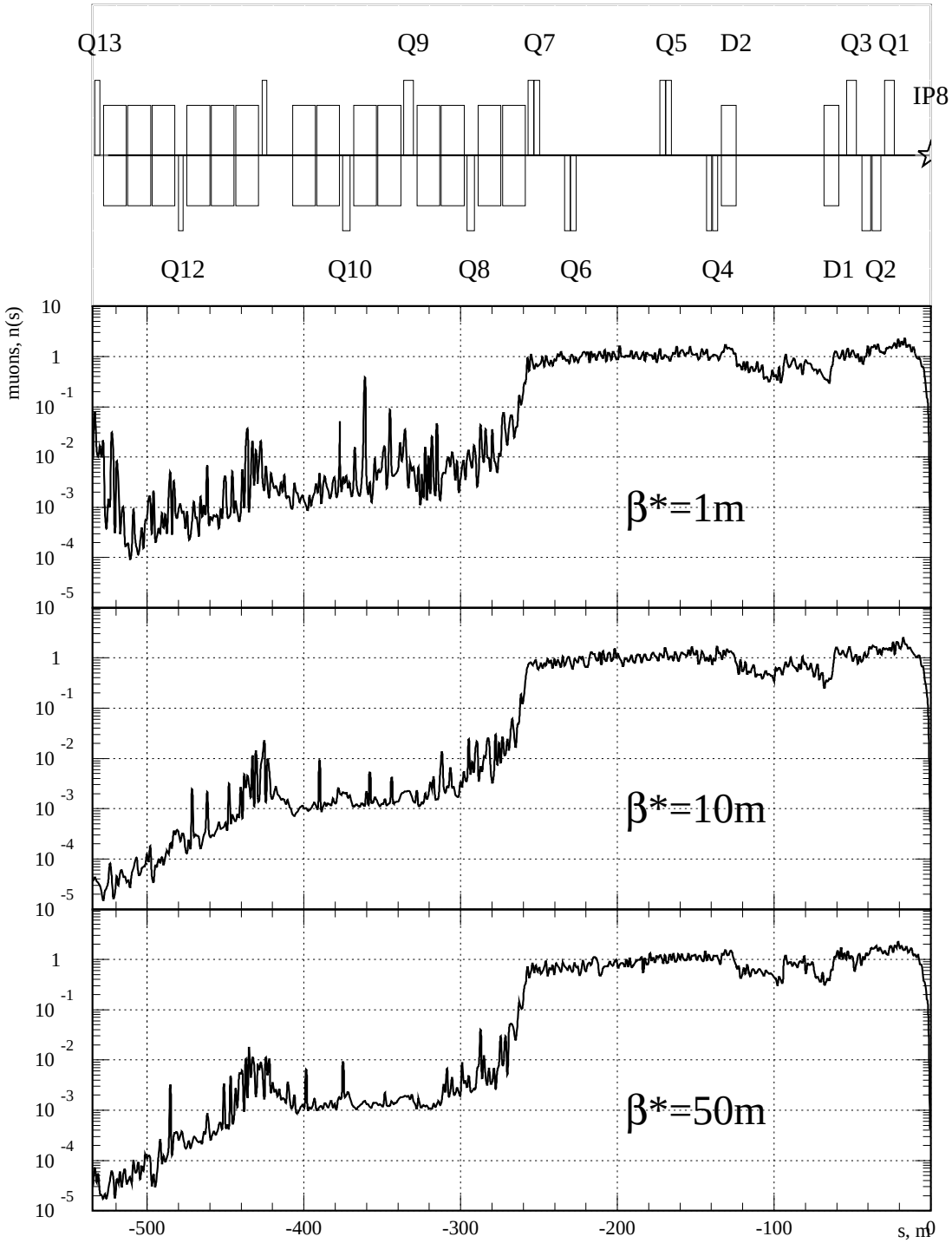

Figure 4: Number of muons, entering the UX85 cavern from the IP1 side, as a function of primary proton–nucleus interaction distance to the IP8, given per unit of linear density of beam–gas interactions.

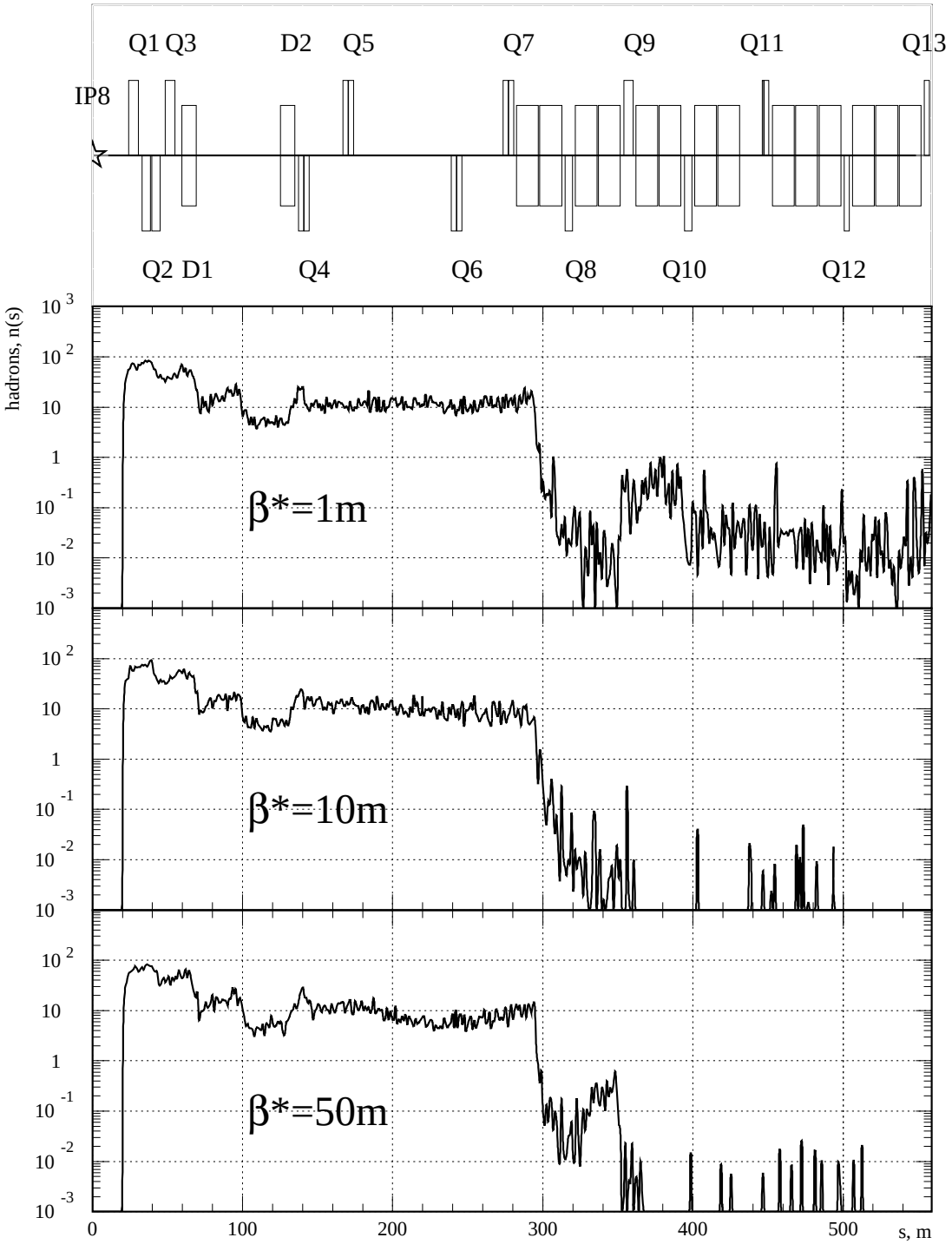

Figure 5: Number of hadrons, entering the UX85 cavern from the injection side, as a function of primary proton–nucleus interaction distance to the IP8, given per unit of linear density of beam–gas interactions.

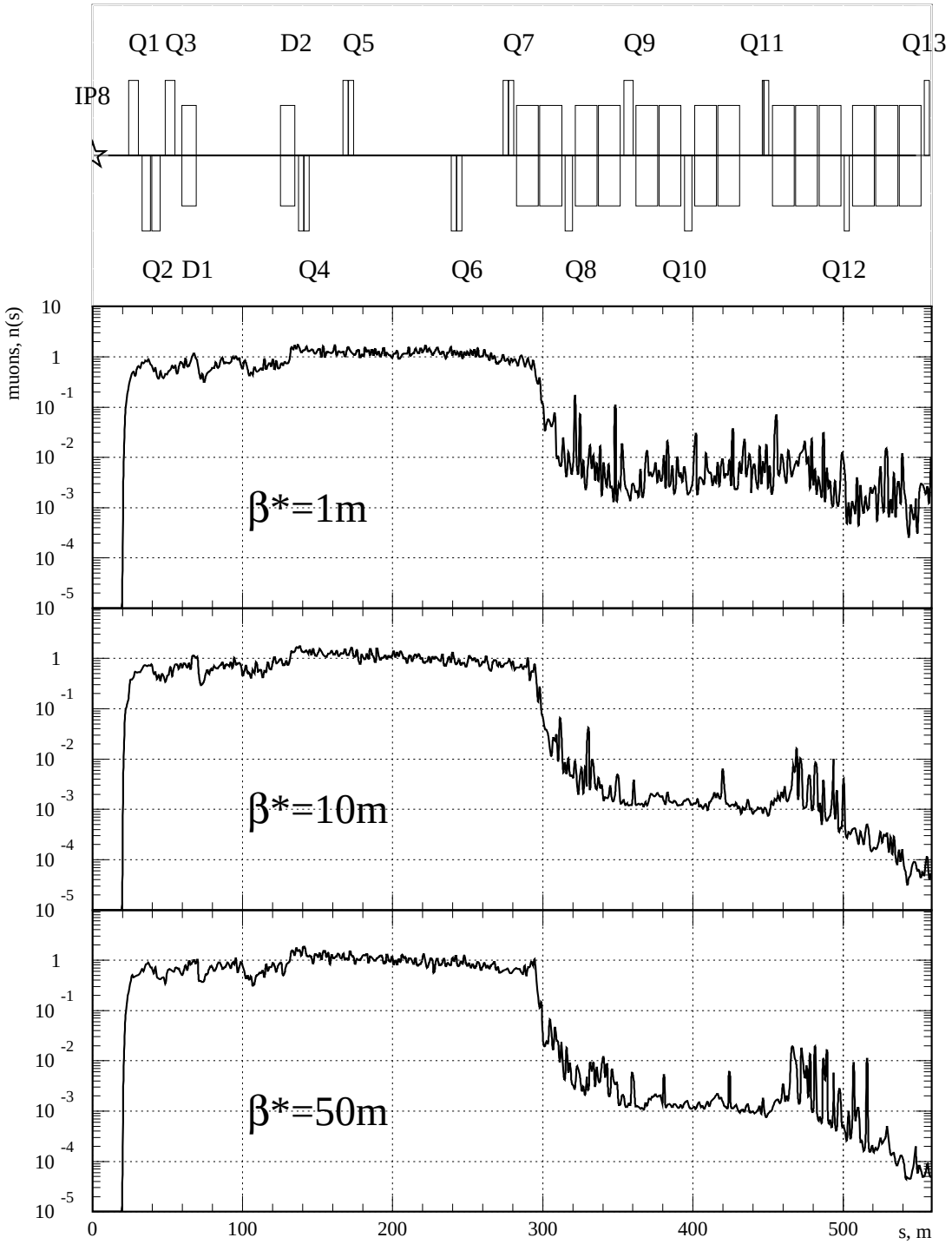

Figure 6: Number of muons, entering the UX85 cavern from the injection side, as a function of primary proton–nucleus interaction distance to the IP8, given per unit of linear density of beam–gas interactions.